Journal of Materials Chemistry A

Accepted Manuscript

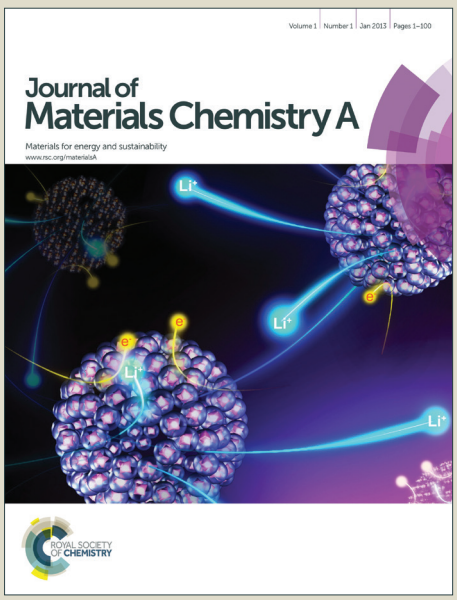

ROYAL SOCIETY OF CHEMISTRY

www.rsc.org/materialsA

Synthesis and characterization of lanthanum silicate oxyapatites co-doped with A (A = Ba, Sr, Ca) and Fe for solid oxide fuel cells

Xiao Guo Cao[a,*] and San Ping Jiang[b**]

[a] School of Materials and Energy, Guangdong University of Technology, Guangzhou 510006, Guangdong, PR China

[b] Fuels and Energy Technology Institute & Department of Chemical Engineering, Curtin University, Perth, WA 6102, Australia

Abstract: The co-doped lanthanum silicate oxyapatites, $La_{9.5}A_{0.5}Si_{5.5}Fe_{0.5}O_{26.5}$ (A = Ba, Sr, Ca), are synthesized by the high-temperature solid state reaction process. The phase formation and structure properties of undoped lanthanum silicate oxyapatite ($La_{9.67}Si_6O_{26.5}$, LSO), Fe-doped lanthanum silicate oxyapatite ($La_{10}Si_5FeO_{26.5}$, LSFO) and co-doped lanthanum silicate oxyapatites ($La_{9.5}A_{0.5}Si_{5.5}Fe_{0.5}O_{26.5}$, A = Ba, Sr, Ca) are characterized by X-ray diffraction (XRD) and scanning electron spectroscopy (SEM). The effect of co-doping of A (A = Ba, Sr, Ca) and Fe on the microstructure, sinterability and oxide ion conductivity of lanthanum silicate oxyapatites are investigated in detail. The results show that, as compared to LSO and LSFO oxyapatites, co-doping of A (A = Ba, Sr, Ca) and Fe significantly benefits the sintering and densification process, and enhances the oxide ion conductivity. For co-doped oxyapatites, the oxide ion conductivities are related to the dopant size, the best properties are obtained for the oxyapatite co-doped with Ca and Fe. The co-doped $La_{9.5}Ca_{0.5}Si_{5.5}Fe_{0.5}O_{26.5}$ (LCSFO) oxyapatite is a good electrolyte for SOFCs, with the oxide ion conductivity of 1.39×10^{-2} S cm^{-1} at 800 ^oC and low activation energy of 90.71 kJ mol^{-1}. The bulk density and oxide ion conductivities of co-doped oxyapatite ceramics increase significantly with the increase of the sintering

* Corresponding author. Tel.: +86-20-39322425; Fax: +86-20-39322570.
E-mail address: xgcao@gdut.edu.cn (X.G. Cao).
** Corresponding author. Tel.: +61 892669804; fax: +61 892661138.
E-mail address: s.jiang@curtin.edu.au (S.P. Jiang).

temperature. The grain bulk and grain boundary resistances of $La_{9.5}Ba_{0.5}Si_{5.5}Fe_{0.5}O_{26.5}$ (LBSFO), $La_{9.5}Sr_{0.5}Si_{5.5}Fe_{0.5}O_{26.5}$ (LSSFO) and LCSFO oxyapatite ceramics are significantly smaller than that of LSO and LSFO oxyapatite ceramics sintered at the identical conditions.

Keywords: Solid oxide fuel cells; Electrolyte; Lanthanum silicate oxyapatite; Co-doping; Oxide ion conductivity

1. Introduction

Oxide ion conducting materials are attracting considerable interest due to a range of environmental-friendly applications, e.g. oxygen sensors, solid oxide fuel cells (SOFCs) and oxygen separation membranes. There is huge amount of literature on materials with perovskite or fluorite-type structures, such as doped ceria, yttria-stabilized zirconia (YSZ) have being developed for applications as the electrolytes for SOFCs [1-3]. Apatite-type lanthanide silicates ($RE_{9.33+x}Si_6O_{26+3x/2}$, RE = rare earth) have been attracting considerable interest as a new class of oxide ion conductors [4-16]. The oxyapatite lattice consists of covalent SiO_4 tetrahedra and ionic-like RE/O channels [17-19]. The RE-site cations occupy cavities created by SiO_4 units with four distinct oxygen positions, additional oxygen sites form channels through the lattice, which are considered as vital for the high oxide ion conduction in these materials [20-22]. Subsequent studies focused on the La containing system, $La_{9.33+x}(SiO_4)_6O_{2+3x/2}$, due to the higher conductivities of this system in comparison to samples containing smaller rare earths. In order to identify strategies for the optimisation of the conductivities, a wide range of doping studies have been performed. These studies showed that nonstoichiometry in the form of either cationic vacancies or oxygen excess was required to achieve good oxide ion conductivities [19, 23-26].

The computer modeling studies have indicated the importance of the silicate substructure in aiding the motion of the oxide ions down the channels in the apatite-type oxide ion conductors. Detailed studies of the Fe-doped lanthanum silicate

oxyapatite systems, $La_{10}Si_{6-x}Fe_xO_{27-x/2}$, have been reported by Kharton et al. [27-29]. T he results showed that as the Fe level increased, an initial increase in conductivity was observed, reaching a maximum value for x = 1.0 ($La_{10}Si_5FeO_{26.5}$). Further Fe incorporation resulted in a decrease in the conductivity up to the fully stoichiometric sample $La_{10}Si_4Fe_2O_{26}$. These results were supported by similar studies on Al and B doping [6, 24, 30, 31]. The doping results as shown above indicate clearly that oxygen over-stoichiometry is responsible for the good oxide-ion conductivity. For oxygen stoichiometric samples containing cationic vacancies [17, 19, 32], a similar doping strategy on the La site ($La_{9.33-2x/3}M_xSi_6O_{26}$, M=Mg, Ca, Sr, Ba) results in a general reduction in the conductivity (e.g. σ (500 ^oC) = 8.3×10^{-5} S cm^{-1} for $La_{8.67}SrSi_6O_{26}$, versus 1.1×10^{-4} S cm^{-1} for $La_{9.33}Si_6O_{26}$) [32], because the number of cationic vacancies is decreased.

Previous doping studies [23, 33-35] show that doping onto the La site with alkaline earth ($La_{10-x}M_xSi_6O_{27-x/2}$, M= Ca, Sr, Ba) enhances the conductivity of lanthanum silicate oxyapatites containing oxygen excess (e.g. σ (700 ^oC) = 1.16×10^{-2} S cm^{-1} for $La_9Ba(SiO_4)_6O_{2.5}$, versus 3.26×10^{-4} S cm^{-1} for $La_{9.33}\square_{0.67}Si_6O_{26}$) [33]. As shown by Nojiri et al. [35], the conductivity of $La_{10-x}Ba_xSi_6O_{27-x/2}$ exhibited a maximum around x = 0.5–0.6. These results show that oxygen excess is more important than cationic vacancies to achieve good oxide-ion conductivity of lanthanum silicate oxyapatite.

The conductivity and chemical stablity was investigated for the La-excess lanthanum silicate oxyapatite with an addition of iron oxide by Mineshige et al.[36-39]. It was revealed that Fe had a positive effect on the conductivity and chemical stablity of Al-doped lanthanum silicate oxyapatite ($La_{10}(Si_{5.8}Al_{0.2})O_{26.9}$) when 0.5 mol% FeOγ was added. It was also found that no La_2SiO_5 and $La(OH)_3$ secondary phases could be identified in the case of the 0.5 mol% FeOγ-added $La_{10}(Si_{5.8}Al_{0.2})O_{26.9}$, though the content of the ion addition was an extremely low level, which indicating that the addition may suppress the secondary phase formation. Besides acting as a dopant into the Si-site, at least a part of Fe ions plays an important role on the mitigation of the degradation of $La_{10}(Si_{5.8}Al_{0.2})O_{26.9}$. Iron oxide might react with the La_2O_3 phase, forming chemically stable $LaFeO_3$ perovskite phase, which improved the chemical

stability of Fe-added $La_{10}(Si_{5.8}Al_{0.2})O_{26.9}$. Thus it would be interesting to study the effect of co-doping of A (A = Ba, Sr, Ca) and Fe on the phase, sinterability and oxide ion conductivity of lanthanum silicate oxyapatite containing oxygen excess.

Recently, $La_{9.5}Ba_{0.5}Si_{5.5}Al_{0.5}O_{26.5}$ was synthesized by using a conventional solid state reaction process [40]. Co-doping lower valent ions on La and Si sites significantly benefit the sintering and densification process. In this paper, $La_{9.5}A_{0.5}Si_{5.5}Fe_{0.5}O_{26.5}$ with A = Ba, Sr, Ca were synthesized by the high-temperature solid state reaction process. The undoped $La_{9.67}Si_6O_{26.5}$ and doped $La_{10}Si_5FeO_{26.5}$ oxyapatites were also studied under identical conditions. The effect of co-doping of A (A = Ba, Sr, Ca) and Fe on the microstructure, sinterability and oxide conductivity of lanthanum silicate oxyapatite were studied by SEM and electrochemical impedance analysis. The results show that co-doping of A (A = Ba, Sr, Ca) and Fe significantly improves the sinterability and oxide ion conductivity of lanthanum silicate oxyapatite.

2. Experimental

2.1. Synthesis of lanthanum silicate oxyapatites powders

The powders were synthesized by a conventional solid state reaction process using high purity La_2O_3, SiO_2, $BaCO_3$, $SrCO_3$, $CaCO_3$and $Fe(NO_3)_3{\cdot}9H_2O$ (all from Sigma–Aldrich) as the raw materials without further treatment. The raw materials were weighed in appropriate ratio to elaborate the compounds with compositions $La_{10}Si_{6.0}O_{26.5}$ (LSO), $La_{10}Si_5FeO_{26.5}$ (LSFO), $La_{9.5}Ba_{0.5}Si_{5.5}Fe_{0.5}O_{26.5}$ (LBSFO), $La_{9.5}Sr_{0.5}Si_{5.5}Fe_{0.5}O_{26.5}$ (LSSFO) and $La_{9.5}Ca_{0.5}Si_{5.5}Fe_{0.5}O_{26.5}$ (LCSFO), and mixed in plastic vessels for 24 h. The details of the following process flow and procedures for the synthesis of apatite powders by solid state reaction can be found in our previous publications [40].

2.2. Characterization

As-synthesized apatite powders were pressed uniaxially into pellets and bars under a pressure of 150 MPa and sintered at 1500, 1550 and 1650 ^oC for 4 h in air. Phase formation of the apatite powders was determined by X-ray diffraction (XRD, Philips MPD 1880) using Cu Kα radiation at room temperature. The microstructure of LSO,

LSFO, LBSFO, LSSFO and LCSFO pellets were examined by scanning electron microscope (SEM, JSM-5600/LV). The bulk densities of the sintered apatites were obtained from the mass and geometric dimensions of the pellet samples. The sintered pellets with ~9 mm in diameter and 1.5 mm in thickness were used for the electrochemical impedance analysis.

The sintered pellets with ~9 mm in diameter and 1.5 mm in thickness were used for the electrochemical impedance analysis. Silver paste (Ferro Corporation USA) was painted onto both sides of the samples as the electrodes. A Solartron 1260 frequency response analyzer in conjunction with a 1287 electrochemical interface was used for the electrochemical impedance spectroscopy (EIS) measurement in the frequency range from 0.1 Hz to 10 M Hz. The EIS measurements were made in 50 ^{o}C interval in air between 300 and 800 ^{o}C.

3. Results and discussion

3.1. XRD and microstructure analysis

Fig. 1 shows the XRD patterns of LSO, LSFO, LBSFO, LSSFO and LCSFO oxyapatite powders calcined at 1300 ^{o}C for 10 h. As lanthanum silica oxyapatites synthesized by solid state reaction route are often contaminated either with La_2SiO_5 or $La_2Si_2O_7$ secondary phases [10, 14, 40-42], the samples are very difficult to obtain with a high purity level. As seen from Fig. 1, a secondary phase, La_2SiO_5, is observed in the XRD patterns of LSO, LSFO and LSSFO oxyapatite powders. And the intensity of La_2SiO_5 secondary phase decreases gradually. The intensity of the La_2SiO_5 phase in the XRD patterns of LSSFO oxyapatite powders is very low, indicating a very small amount of the La_2SiO_5 second phase. However, no La_2SiO_5 phase is observed in the XRD patterns of LBSFO and LCSFO oxyapatite powders. Doping Fe on the Si site for LSO oxyapatite significantly suppresses the the formation of La_2SiO_5 secondary phase, similar to the effect of the addition of 0.5 mol% FeOγ to $La_{10}(Si_{5.8}Al_{0.2})O_{26.9}$ [38]. The added Fe ions might suppress formation of La-rich secondary phases due to additional dissolution of La ions into the oxyapatite phase through the incorporation of Fe ions into the Si-sites. The results also indicate that doping A (A = Ba, Sr, Ca) on

the La site for LSFO oxyapatite further prevents the formation of La_2SiO_5 secondary phase.

As shown in Fig. 1, the peak positionsare are affected by the doped elements. When iron dopes lanthanum silicate oxyapatite, the radius of Fe^{3+} cations is larger than Si^{4+}, which could result in the expansion of unit cell [27], indicating by the shift of the XRD diffraction peaks of LSFO to a lower value in comparison to LSO. The XRD diffraction peaks of LBSFO shift to a lower value in comparison to LSFO, because the ionic radius of Ba^{2+} is larger than that of La^{3+}, which leads to increasing unit cell volume [43]. The radius of Ca^{2+} cations is smaller than Ba^{2+} and the unit cell contracts, being indicated by the shift of the XRD diffraction peaks of LCSFO to a higher value in comparison to LBSFO. Such results on alkaline elements (Ba, Sr, Ca) doped lanthanum silicates in this study are in consistent with the shifts in lattice parameters observed in other studies [33, 34, 44].

3.2. Microstructure and densification analysis

Fig. 2 shows the surface SEM micrographs of LBSFO oxyapatite pellets sintered at different temperatures from the oxyapatite powders calcined at 1300 ^oC for 10 h. SEM observation shows that the porosity of LBSFO oxyaptites decreases with the increase of the sintering temperature. The grains size of LBSFO oxyapatites increase with the increase of sintering temperature. When the sintering temperature increased to 1600 ^oC, the microstructure of LBSFO oxyapatite shows denser structure with no porosity and larger grains. These indicate that the densification process of LBSFO oxyapatite depends strongly on the sintering temperature.

Fig. 3 shows the surface SEM micrographs of (a) LSO, (b) LSFO, (c) LSSFO and (d) LCSFO apatite pellets sintered at 1550 ^oC from the oxyapatite powders calcined at 1300 ^oC for 10 h. SEM observation shows that LSO electrolyte sample is very porous, however, LSFO oxyapatite sample shows much denser structures with less porosity. The microstructures of the co-doped oxyapatite samples show compact structures with substantially reduced porosity (Fig. 2b and 3). In addition to the increased densification, co-doping of A (A = Ba, Sr, Ca) and Fe also produces the oxyapatite pellets with uniform grain size. The results indicate that co-doping of A (A = Ba, Sr,

Ca) and Fe significantly enhances the sintering and densification process.

The significant differences in the microstructure of the LSO, LSFO, LBSFO, LSSFO and LCSFO oxyapatite ceramics are also indicated by the bulk density of the oxyapatite ceramics sintered at 1550 ^{o}C, as shown in Fig. 4. As evident from Fig. 4, the bulk densities of LBSFO, LSSFO and LCSFO are 5.21, 5.14 and 5.43 g cm^{-3}, respectively, which are significantly higher than 4.74 g cm^{-3} of LSFO, consistent with the SEM observation. On the other hand, the bulk density of of LSFO is higher than that of LSO (4.02 g cm^{-3}). The bulk densities of the oxyapatite ceramics also indicate that co-doping of A (A = Ba, Sr, Ca) and Fe is advantageous in enhancing the densification of oxyapatite ceramics.

3.3. Impedance and conductivity properties

The conductivities of LSO, LSFO, LBSFO, LSSFO and LCSFO oxyapatite ceramics sintered at different temperatures were investigated by electrochemical impedance spectroscopy in temperature range of 300–800 ^{o}C. Fig. 5 shows the complex impedance plots of (a) LSO, (b) LSFO, (c) LBSFO, (d) LSSFO and (e) LCSFO oxyapatites sintered at 1550 ^{o}C. The EIS was measured at 800 ^{o}C. The impedance behaviors of LSO, LSFO, LBSFO, LSSFO and LCSFO oxyapatite ceramics are characterized by a large depressed curve, indicating the dominance of the electrode process. The impedance of LSFO oxyapatite is significantly lower than that of LSO, however, higher than that of LBSFO, LSSFO and LCSFO oxyapatites under identical test conditions. This indicates that co-doping of A (A = Ba, Sr, Ca) and Fe obviously enhances the oxide ion conductivity of lanthanum silicate oxyapatite, which is mostly due to the fact that co-doping of A (A = Ba, Sr, Ca) and Fe for lanthanum silicate oxyapatite significantly benefits the sintering and densification process and prevents the formation of La_2SiO_5 secondary phase.

Fig. 6 shows the oxide ion conductivities of LSO, LSFO, LBSFO, LSSFO and LCSFO oxyapatite ceramics sintered at 1500, 1550 and 1600 ^{o}C, measured at 800 ^{o}C. The oxide ion conductivities of LBSFO, LSSFO and LCSFO oxyapatites are higher than that of LSO and LSFO oxyapatites sintered at the same temperature, which is most likely due to the higher densification and less or no La_2SiO_5 impurity of LBSFO,

LSSFO and LCSFO. As seen from Fig. 6, the oxide ion conductivity of the oxyapatie ceramics increases considerably with the increase of sintering temperature, which is likely due to the higher densification of the oxyapatite ceramics sintered at higher temperature (Fig. 2). For example, as the sintering temperature increased from 1500 to 1600 ^{o}C, the oxide ion conductivity of LBSFO is increased from 1.05×10^{-2} to 1.25×10^{-2} S cm^{-1}.

Fig. 7 presents the complex impedance plots obtained for LSO, LSFO, LBSFO, LSSFO and LCSFO oxyapatite ceramics sintered at 1550 ^{o}C. The EIS was measured at 500 ^{o}C. The oxyapatite powders were calcined at 1300 ^{o}C for 10 h. Fig. 8 shows the distribution of grain bulk and grain boundary resistances of LSO, LSFO, LBSFO, LSSFO and LCSFO oxyapatite ceramics sintered at 1550 ^{o}C, measured at 500 ^{o}C. As shown from Fig. 7, the complex impedance plots of the oxyapatite materials consists of two semicircular arcs from high to low frequency that can be identified with the grain bulk (R_g) and grain boundary (R_{gb}) resistances. The symbols are the experimental data and lines are the fitted results based on equivalent circuit with two RQ (R: resistance; Q: constant phase element) elements in series [14, 34, 41, 45]. In addition, a diffusion-limited process leads to an impedance response (Warburg impedance Z_w) that appear as a small tail or arc at lower frequencies [14]. However, the grain bulk and grain boundary arcs disappear with further increasing the measuring temperature. As the measuring temperature is increased, the time constants of the relaxations resulting from the individual polarizations are reduced and hence the arcs are shifted to higher frequencies. Finally, only the electrode contribution is visible at higher measuring temperatures (Fig. 5). The impedance arcs of LBSFO, LSSFO and LCSFO are significantly smaller than that of LSO and LSFO sintered at the same temperatures. The grain bulk and grain boundary resistances of LBSFO, LSSFO and LCSFO oxyapatite ceramics are significantly smaller than that of LSO and LSFO oxyapatite ceramics. The reduction of grain bulk resistance of LBSFO, LSSFO and LCSFO oxyapatites is perhaps attributed to less or no La_2SiO_5 impurity (Fig. 1). Co-doping of A (A = Ba, Sr, Ca) and Fe significantly enhances the sintering and densification process, which results in denser structure and larger grains. Therefore,

the grain boundaries of the co-doped oxyapatites are reduced, which leads to the rduction of the grain boundary resistance.

Fig. 9 shows the impedance curves of LBSFO oxyapatite ceramic sintered at 1550 ^{o}C. The EIS was measured at 300 ^{o}C. As shown from Fig. 9, the complex impedance plots of LBSFO consists of three different contributions. The high and medium frequency arcs can be clearly separated by the frequency range, and identified with the grain bulk (R_g) and grain boundary (R_{gb}) resistances, respectively. In addition, a small tail at low frequencies (below 1Hz) correspond to the electrode interface diffusion. As shown from Fig.7c and Fig. 9 for the impedance curves LBSFO sintered at 1550 ^{o}C, the grain bulk and grain boundary arcs move to the low frequency region at lower measuring temperature. And the grain boundary resistance increases visibly with the decrease of measuring temperature, indicating the dominance of grain boundary resistance to the oxide ion resistivity of LBSFO oxyapatite electrolyte at low measuring temperatures.

Fig. 10 shows the activation energy plots of LSO, LSFO, LBSFO, LSSFO and LCSFO oxyapatite electrolytes sintered at 1550 ^{o}C. The oxide ion conductivities and activation energies of the lanthanum silicate oxyapatites are listed in Table 1. As seen from Table 1 and Fig.10, the activation energies of LBSFO, LSSFO and LCSFO oxyapatites are lower than that of LSO oxyapatite. On the other hand, the oxide ion conductivities of LBSFO, LSSFO and LCSFO oxyapatites are higher than that of LSO and LSFO oxyapatites under identical test conditions. For example, the oxide ion conductivities of LBSFO, LSSFO and LCSFO are 1.18×10^{-2}, 1.37×10^{-2} and 1.39×10^{-2} S cm^{-1} at 800 ^{o}C, respectively, which are higher than 5.30×10^{-3} S cm^{-1} of LSO and 8.16×10^{-3} S cm^{-1} of LSFO. The best oxide ion conductivity at 800 ^{o}C and the lowest activation energy are observed for LCSFO (1.39×10^{-2} S cm^{-1} at 800 ^{o}C and 90.71 kJ mol^{-1}). These results indicate that co-doping of A (A = Ba, Sr, Ca) and Fe obviously enhances the oxide ion conductivity and decrease the activation energy of lanthanum silicate oxyapatite.

4. Conclusions

LSO, LSFO, LBSFO, LSSFO and LCSFO oxyapatite samples were synthesized by solid state reaction process. The comparison of undoped LSO oxyapatite, doped LSFO oxyapatite and co-doped $La_{9.5}A_{0.5}Si_{5.5}Fe_{0.5}O_{26.5}$ (A = Ba, Sr, Ca) oxyapatites revealed that co-doping of A (A = Ba, Sr, Ca) and Fe significantly benefits the sintering and densification process, and enhances the oxide ion conductivity. For co-doped oxyapatites, the oxide ion conductivities and activation energy are related to the dopant size. The best properties are obtained for the co-doped $La_{9.5}Ca_{0.5}Si_{5.5}Fe_{0.5}O_{26.5}$ (LCSFO) oxyapatite, with the oxide ion conductivity of 1.39×10^{-2} S cm^{-1} at 800 ^{o}C and low activation energy of 90.71 kJ mol^{-1}. Moreover, the sintering temperature has great effect on the oxide ion conductivity and microstructures. The oxide ion conductivity, bulk density and grain size of co-doped oxyapatite ceramics increase significantly with the increase of the sintering temperature.

The grain bulk and grain boundary resistances of LBSFO, LSSFO and LCSFO oxyapatite ceramics are significantly smaller than that of LSO and LSFO oxyapatite ceramics sintered at the identical conditions. The reduction of grain bulk and grain boundary resistances for LBSFO, LSSFO and LCSFO oxyapatites is mostly attributed to no or less formation of La_2SiO_5 secondary phase and denser microstructure with larger grains. The results in the present study demonstrate that co-doping of A (A = Ba, Sr, Ca) and Fe improves the sinterability and oxide ion conductivity of lanthanum silicate oxyapatite.

Acknowledgement

This work is supported by the National Natural Science Foundation of China(Grant No. 51302042), the Guangdong Provincial Natural Science Foundation of China (Grant No. S2012010010140), the Pearl River New Star Plan of Science and Technology of Guangzhou City of China (Grant No. 2013J2200038), and the Australian Research Council *Linkage Project* funding scheme (project number: LP110200281).

References:

1. J. B. Goodenough, *Annual Review of Materials Research*, 2003, 33, 91-128.
2. T. Talebi, M. Haji and B. Raissi, *International Journal of Hydrogen Energy*, 2010, 35, 9420-9426.
3. J. Y. Park and E. D. Wachsman, *Ionics*, 2006, 12, 15-20.
4. S. Nakayama, T. Kageyama, H. Aono and Y. Sadaoka, *Journal of Materials Chemistry*, 1995, 5, 1801-1805.
5. S. Nakayama and M. Sakamoto, *Journal of the European Ceramic Society*, 1998, 18, 1413-1418.
6. E. J. Abram, D. C. Sinclair and A. R. West, *J. Mater. Chem.*, 2001, 11, 1978-1979.
7. E. Bechade, I. Julien, T. Iwata, O. Masson, P. Thomas, E. Champion and K. Fukuda, *Journal of the European Ceramic Society*, 2008, 28, 2717-2724.
8. L. Leon-Reina, E. R. Losilla, M. Martinez-Lara, S. Bruque and M. A. G. Aranda, *Journal of Materials Chemistry*, 2004, 14, 1142-1149.
9. T. Liao, T. Sasaki, S. Suehara and Z. Sun, *Journal of Materials Chemistry*, 2011, 21, 3234-3242.
10. Y. Masubuchi, M. Higuchi, T. Takeda and S. Kikkawa, *Solid State Ionics*, 2006, 177, 263-268.
11. H. Okudera, Y. Masubuchi, S. Kikkawa and A. Yoshiasa, *Solid State Ionics*, 2005, 176, 1473-1478.
12. E. Kendrick, D. Headspith, A. Orera, D. C. Apperley, R. I. Smith, M. G. Francesconi and P. R. Slater, *Journal of Materials Chemistry*, 2009, 19, 749-754.
13. S. Zec, J. Dukic, M. Pusevac, S. Boskovic and R. Petrovic, *Materials and Manufacturing Processes*, 2009, 24, 1104-1108.
14. B. Li, W. Liu and W. Pan, *Journal of Power Sources*, 2010, 195, 2196-2201.
15. X. G. Cao and S. P. Jiang, *International Journal of Hydrogen Energy*, 2013, 38, 2421-2431.
16. S. Chefi, M. Kahlaoui, A. Inoubli, A. Madani and A. Hammou, *Ceramics International*, 2013, 39, 4507-4512.
17. J. E. H. Sansom, D. Richings and P. R. Slater, *Solid State Ionics*, 2001, 139, 205-210.
18. J. E. H. Sansom, J. R. Tolchard, M. S. Islam, D. Apperley and P. R. Slater, *J. Mater. Chem.*, 2006, 16, 1410-1413.
19. J. R. Tolchard, M. S. Islam and P. R. Slater, *J. Mater. Chem.*, 2003, 13, 1956-1961.
20. E. Kendrick, M. S. Islam and P. R. Slater, *Journal of Materials Chemistry*, 2007, 17, 3104-3111.
21. J. E. H. Sansom and P. R. Slater, *Solid State Ionics*, 2004, 167, 23-27.
22. S. W. Tao and J. T. S. Irvine, *Materials Research Bulletin*, 2001, 36, 1245-1258.
23. P. R. Slater and J. E. H. Sansam, in *Solid State Chemistry V*, eds. P. Sajgalik, M. Drabik and S. Varga, 2003, vol. 90-91, pp. 195-200.
24. A. Najib, J. E. H. Sansom, J. R. Tolchard, P. R. Slater and M. S. Islam, *Dalton Transactions*, 2004, 3106-3109.
25. S. Nakayama and M. Highchi, *Journal of Materials Science Letters*, 2001, 20, 913-915.

26. S. Nakayama, M. Sakamoto, M. Highchi and K. Kodaira, *Journal of Materials Science Letters*, 2000, 19, 91-93.
27. V. V. Kharton, A. L. Shaula, M. V. Patrakeev, J. C. Waerenborgh, D. P. Rojas, N. P. Vyshatko, E. V. Tsipis, A. A. Yaremchenko and F. M. B. Marques, *Journal of the Electrochemical Society*, 2004, 151, A1236-A1246.
28. A. L. Shaula, V. V. Kharton, J. C. Waerenborgh, D. P. Rojas and F. M. B. Marques, *Journal of the European Ceramic Society*, 2005, 25, 2583-2586.
29. J. McFarlane, S. Barth, M. Swaffer, J. E. H. Sansom and P. R. Slater, *Ionics*, 2002, 8, 149-154.
30. A. L. Shaula, V. V. Kharton and F. M. B. Marques, *Solid State Ionics*, 2006, 177, 1725-1728.
31. A. L. Shaula, V. V. Kharton and F. M. B. Marques, *Journal of Solid State Chemistry*, 2005, 178, 2050-2061.
32. J. E. H. Sansom, E. Kendrick, J. R. Tolchard, M. S. Islam and P. R. Slater, *Journal of Solid State Electrochemistry*, 2006, 10, 562-568.
33. S. Beaudet-Savignat, A. Vincent, S. Lambert and F. Gervais, *Journal of Materials Chemistry*, 2007, 17, 2078-2087.
34. L. Zhang, H. Q. He, H. Wu, C.-Z. Li and S. P. Jiang, *International Journal of Hydrogen Energy*, 2011, 36, 6862-6874.
35. Y. Nojiri, S. Tanase, M. Iwasa, H. Yoshioka, Y. Matsumura and T. Sakai, *Journal of Power Sources*, 2010, 195, 4059-4064.
36. A. Mineshige, Y. Ohnishi, R. Sakamoto, Y. Daiko, M. Kobune, T. Yazawa, H. Yoshioka, T. Nakao, T. Fukutsuka and Y. Uchimoto, *Solid State Ionics*, 2011, 192, 195-199.
37. Y. Ohnishi, A. Mineshige, Y. Daiko, M. Kobune, H. Yoshioka and T. Yazawa, *Solid State Ionics*, 2010, 181, 1697-1701.
38. A. Mineshige, H. Mieda, M. Manabe, T. Funahashi, Y. Daiko, T. Yazawa, M. Nishi, K. Yamaji, T. Horita, K. Amezawa, K. Yashiro, T. Kawada and H. Yoshioka, *Solid State Ionics*, 2014, 262, 555-558.
39. A. Mineshige, T. Nakao, Y. Ohnishi, R. Sakamoto, Y. Daiko, M. Kobune, T. Yazawa, H. Yoshioka, T. Fukutsuka and Y. Uchimoto, *Journal of the Electrochemical Society*, 2010, 157, B1465-B1470.
40. X. G. Cao and S. P. Jiang, *Journal of Alloys and Compounds*, 2012, 523, 127-133.
41. J. Xiang, Z.-G. Liu, J.-H. Ouyang and F.-Y. Yan, *Electrochimica Acta*, 2012, 65, 251-256.
42. L. Leon-Reina, M. C. Martin-Sedeno, E. R. Losilla, A. Cabeza, M. Martinez-Lara, S. Bruque, F. M. B. Marques, D. V. Sheptyakov and M. A. G. Aranda, *Chemistry of Materials*, 2003, 15, 2099-2108.
43. K. P. Ong, P. Wu, L. Liu and S. P. Jiang, *Applied Physics Letters*, 2007, 90.
44. S. Lambert, A. Vincent, E. Bruneton, S. Beaudet-Savignat, F. Guillet, B. Minot and F. Bouree, *Journal of Solid State Chemistry*, 2006, 179, 2602-2608.
45. S. P. Jiang, J. G. Love and Y. Ramprakash, *Journal of Power Sources*, 2002, 110, 201-208.

Table 1 Conductivities and activation energies of LSO, LSFO, LBSFO, LSSFO and LCSFO oxyapatite electrolytes

Samples	Conductivity (S cm^{-1})				E_a ($kJ\ mol^{-1}$)
	300	500	700	800	
LSO	7.20×10^{-7}	7.06×10^{-5}	1.83×10^{-3}	5.30×10^{-3}	98.29
LSFO	2.37×10^{-6}	1.96×10^{-4}	3.80×10^{-3}	8.16×10^{-3}	90.91
LBSFO	2.62×10^{-6}	4.03×10^{-4}	4.84×10^{-3}	1.18×10^{-2}	92.58
LSSFO	3.40×10^{-6}	3.33×10^{-4}	6.19×10^{-3}	1.37×10^{-2}	93.29
LCSFO	4.09×10^{-6}	3.87×10^{-4}	6.28×10^{-3}	1.39×10^{-2}	90.71

Figure captions:

1. XRD patterns of LSO, LSFO, LBSFO, LSSFO and LCSFO powders calcined at 1300 ^{o}C for 10 h in air.
2. SEM micrographs of the surface of (a, b, c) LBSFO apatite pellets sintered at 1500, 1550 and 1600 ^{o}C for 4 h in air, respectively. The oxyapatite powders were calcined at 1300 ^{o}C for 10 h.
3. SEM micrographs of the surface of (a) LSO, (b) LSFO, (c) LSSFO and (d) LCSFO apatite pellets sintered at 1550 ^{o}C for 4 h in air. The oxyapatite powders were calcined at 1300 ^{o}C for 10 h.
4. Bulk density of LSO, LSFO, LBSFO, LSSFO and LCSFO ceramics sintered at 1550 ^{o}C for 4 h in air. The oxyapatite powders were calcined at 1300 ^{o}C for 10 h.
5. Complex impedance plots of (a) LSO, (b) LSFO, (c) LBSFO, (d) LSSFO and (e) LCSFO oxyapatite electrolytes sintered at 1600 ^{o}C for 4 h in air. EIS was measured at 800 ^{o}C. Numbers are frequencies in Hz. The oxyapatite powders were calcined at 1300 ^{o}C for 10 h.
6. Plots of total conductivity values measured at 800 ^{o}C for LSO, LSFO, LBSFO, LSSFO and LCSFO oxyapatite electrolytes as a function of sintering temperature. The oxyapatite powders were calcined at 1300 ^{o}C for 10 h.
7. Complex impedance plots of (a) LSO, (b) LSFO, (c) LBSFO, (d) LSSFO and (e) LCSFO oxyapatite electrolytes sintered at 1550 ^{o}C for 4 h in air. The oxyapatite powders were calcined at 1300 ^{o}C for 10 h. EIS was measured at

500 ^{o}C and numbers are frequencies in Hz. The symbols are the measured data and the lines are the fitting results.

8. Grain bulk and grain boundary resistances measured at 500 ^{o}C of LSO, LSFO, LBSFO, LSSFO and LCSFO oxyapatite electrolytes sintered at 1550 ^{o}C for 4 h in air.
9. Complex impedance plots of LBSFO oxyapatites sintered at 1550 ^{o}C for 4 h in air. EIS was measured at 300 ^{o}C. Numbers are frequencies in Hz. The oxyapatite powders were calcined at 1300 ^{o}C for 10 h.
10. Activation energy plots of LSO, LSFO, LBSFO, LSSFO and LCSFO oxyapatite specimens sintered at 1550 ^{o}C for 4 h in air.

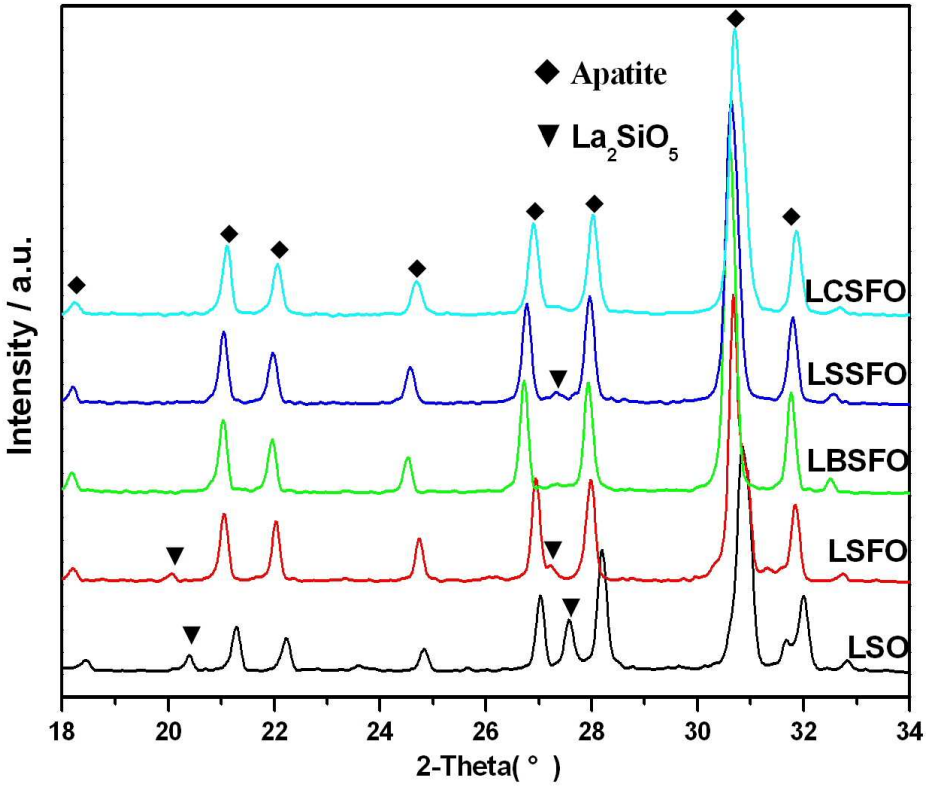

Figure 1

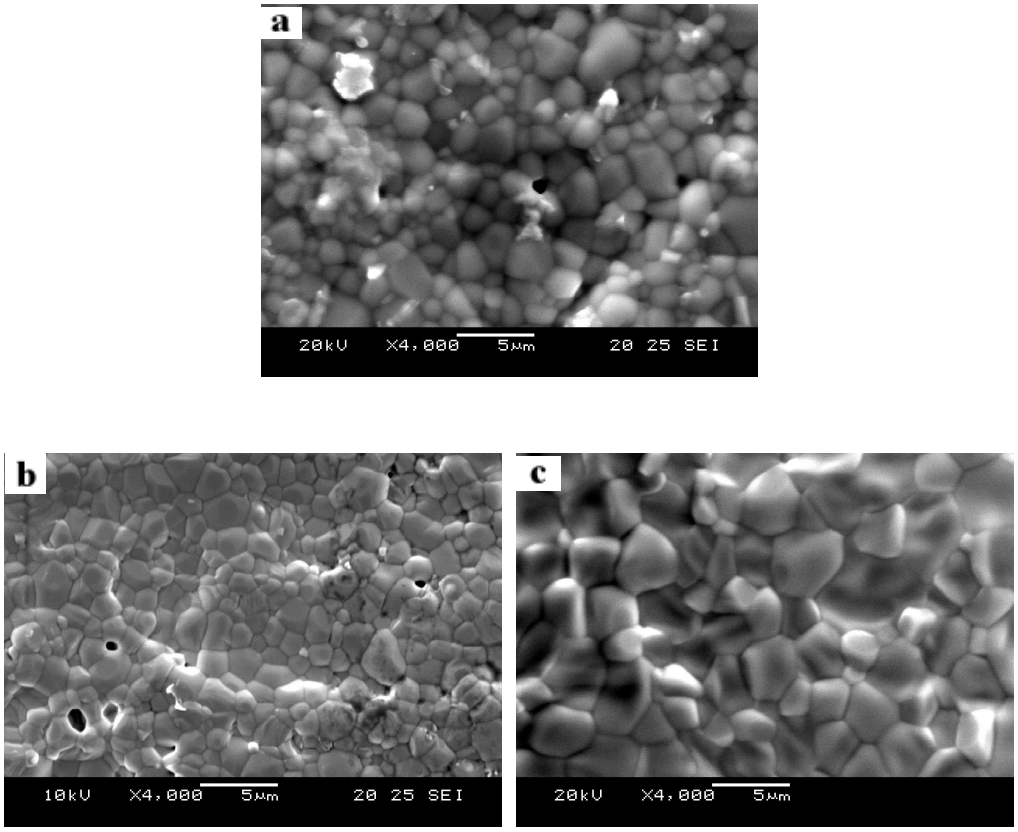

Figure 2

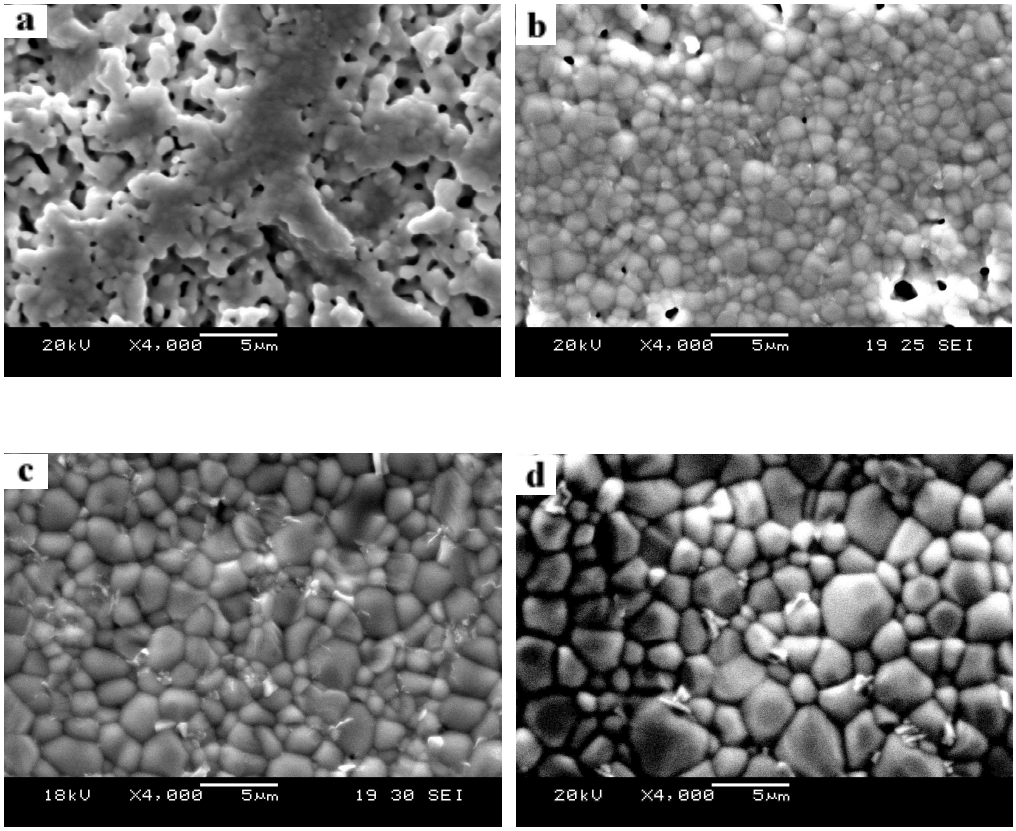

Figure 3

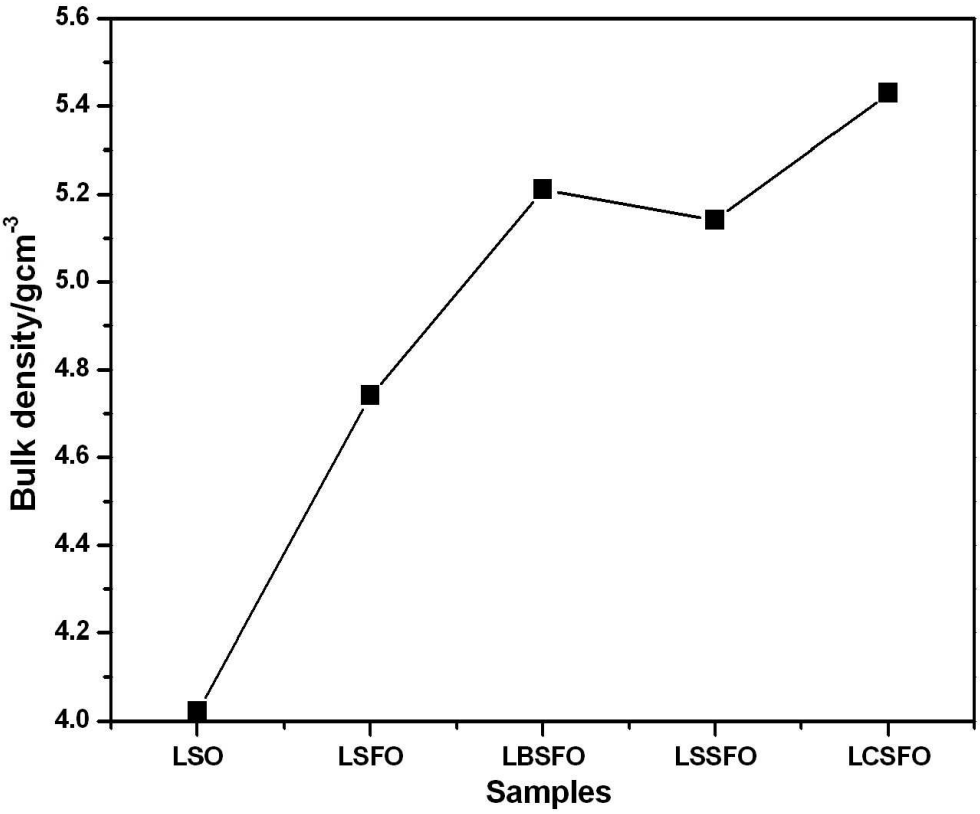

Figure 4

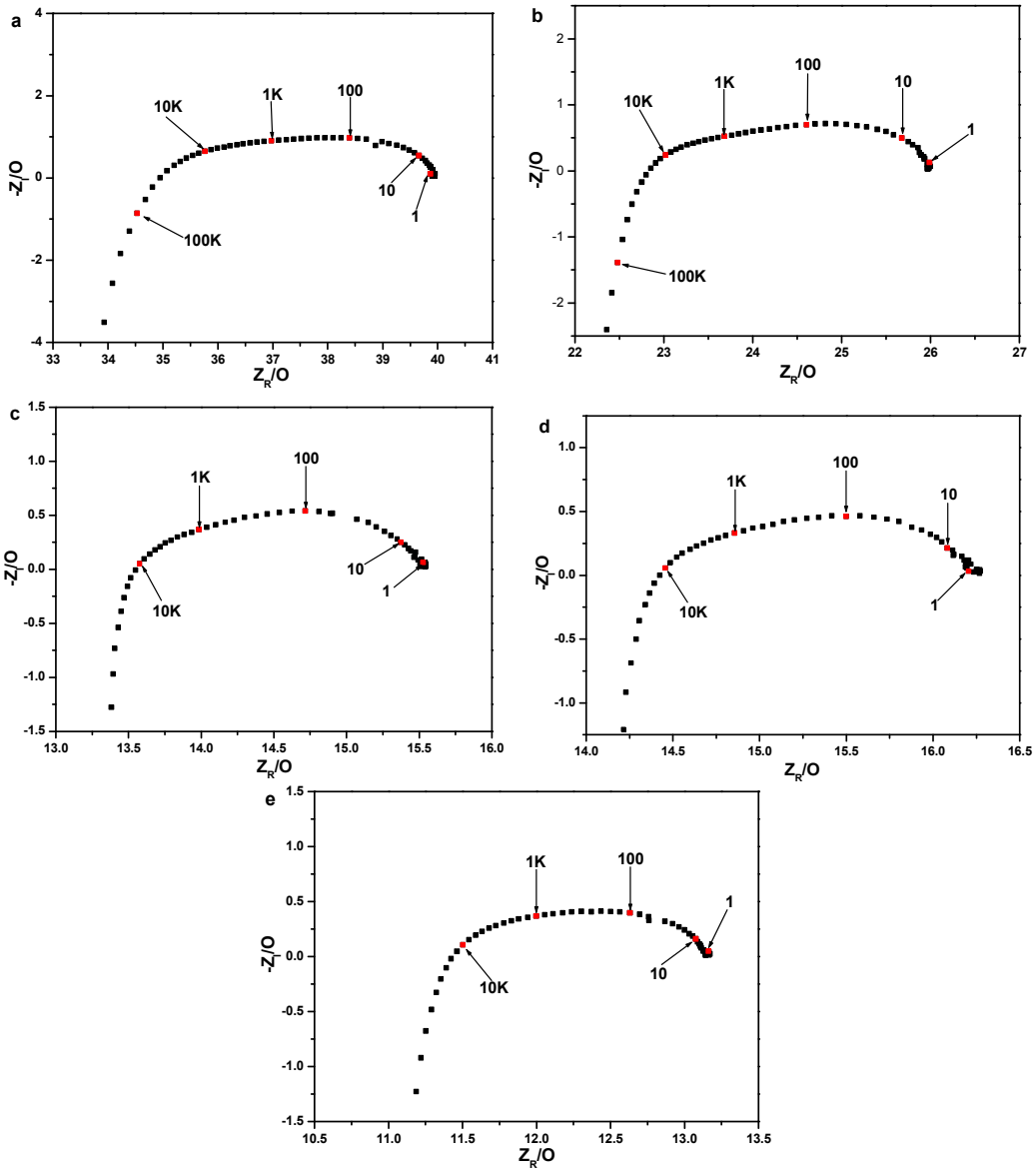

Figure 5

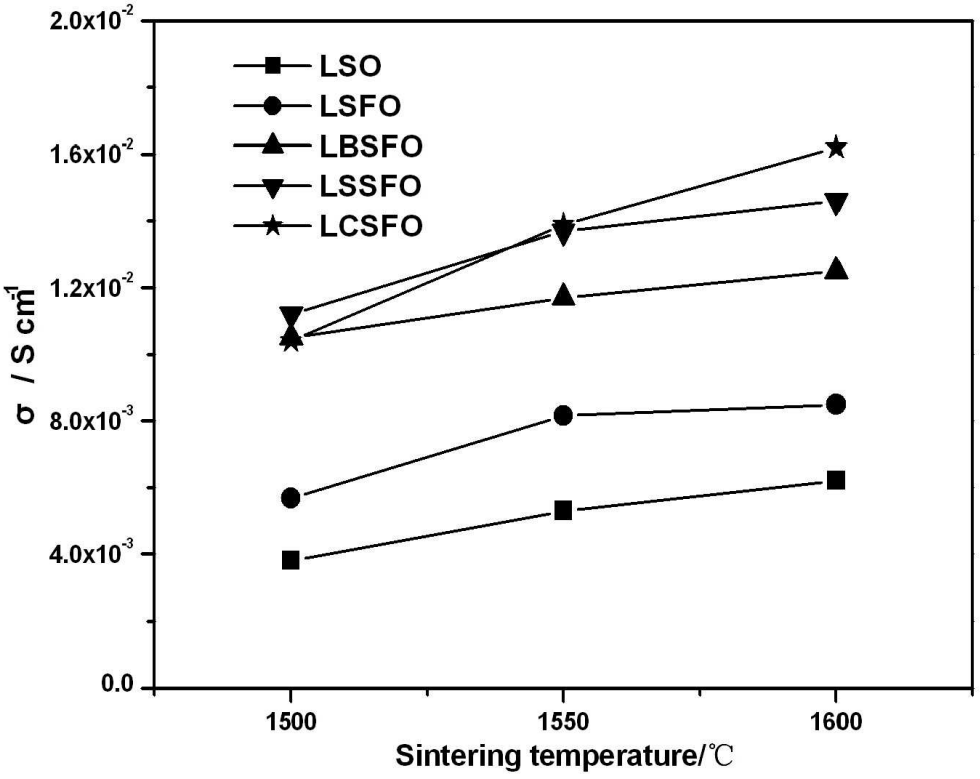

Figure 6

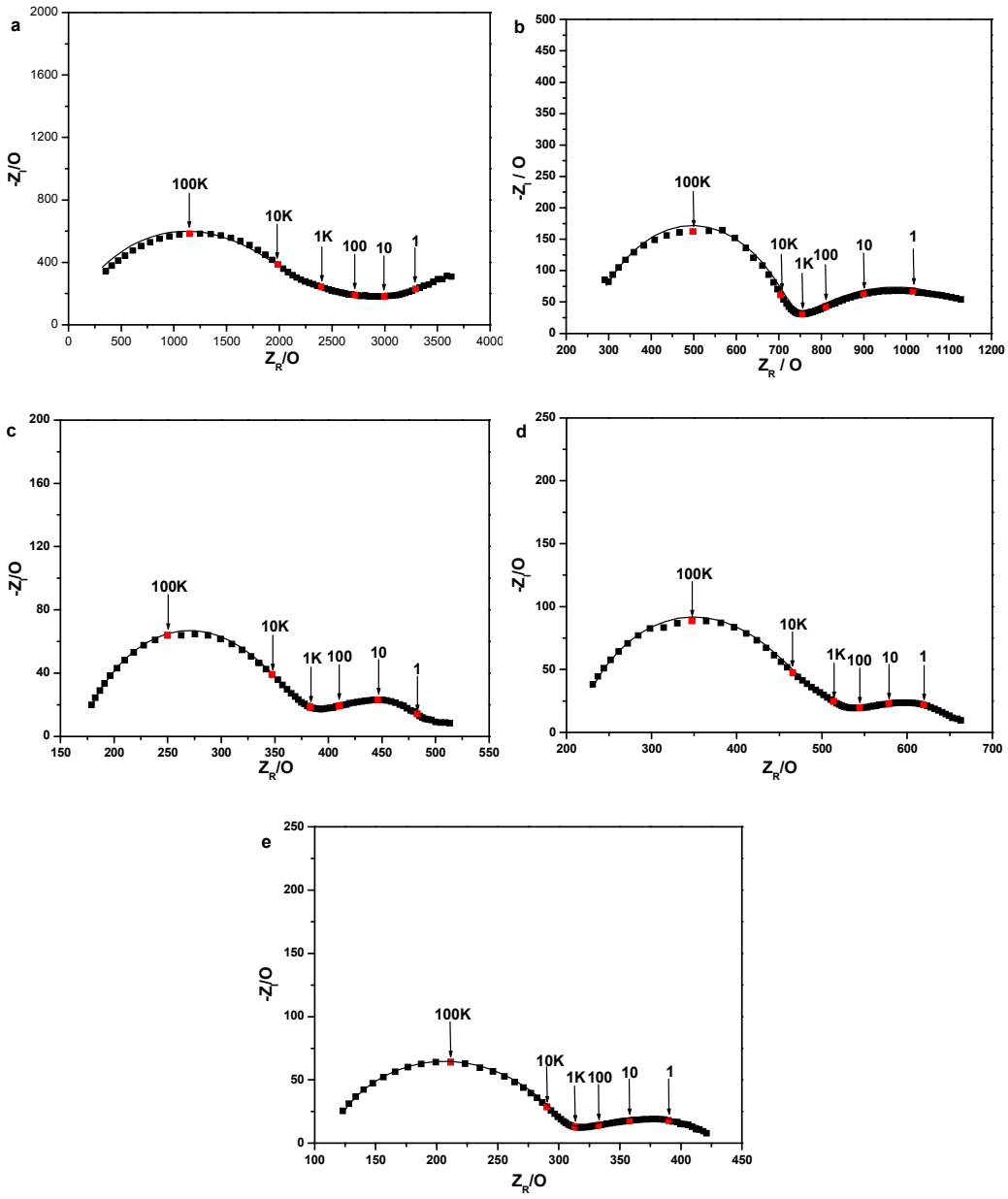

Figure 7

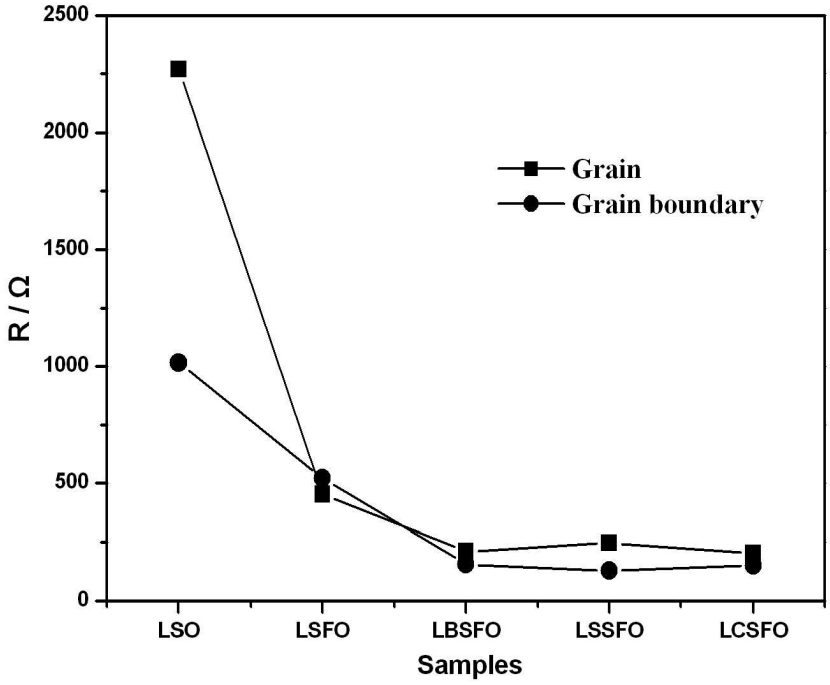

Figure 8

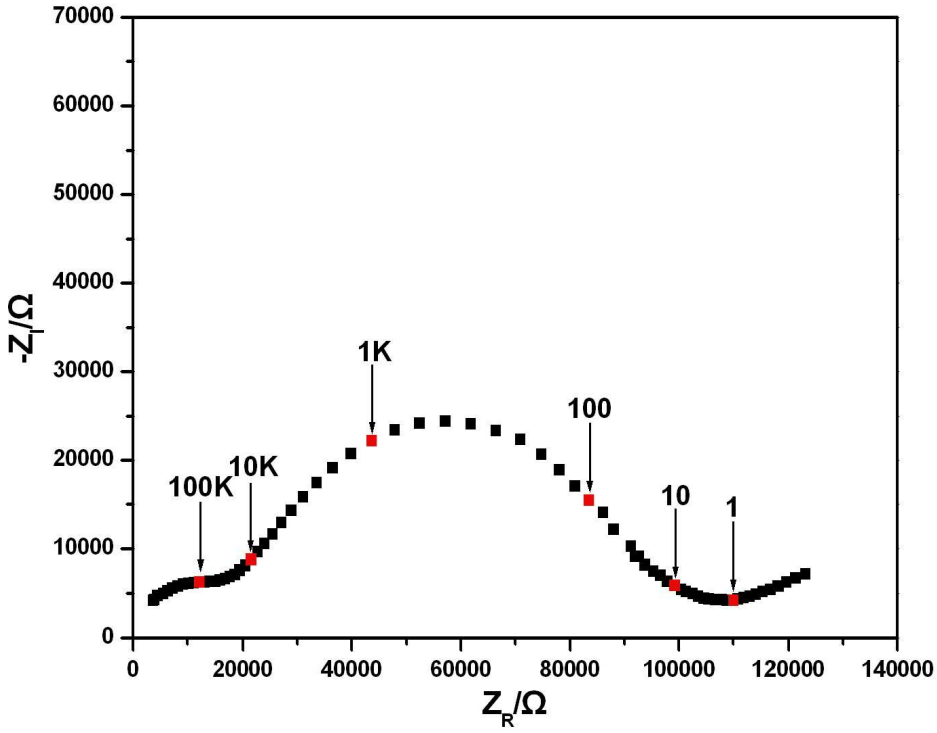

Figure 9

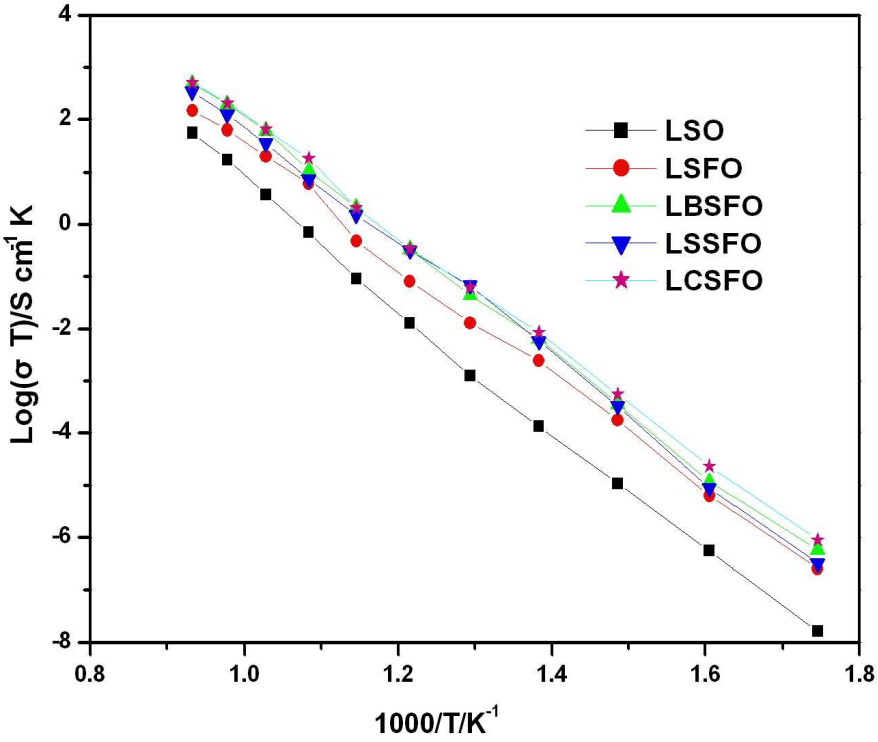

Figure 10